Nanoparticle surfactants for kinetically-arrested photoactive assemblies to track light-induced electron transfer

Kamil Sokołowski,[1,2,†] Junyang Huang,[3,†] Tamás Földes,[4,6] Jade A. McCune,[1] David D. Xu,[1] Bart de Nijs,[3] Rohit Chikkaraddy,[3] Sean M. Collins,[5] Edina Rosta,[4,6] Jeremy J. Baumberg,[3] & Oren A. Scherman[1]

[1]*Melville Laboratory for Polymer Synthesis, Department of Chemistry, University of Cambridge, Lensfield Road, Cambridge CB2 1EW, United Kingdom.*

[2]*Institute of Physical Chemistry, Polish Academy of Science, Kasprzaka 44/52, 01-224 Warsaw, Poland.*

[3]*NanoPhotonics Centre, Cavendish Laboratory, University of Cambridge, Cambridge CB3 0HE, United Kingdom.*

[4]*Department of Chemistry, King's College London, 7 Trinity Street, SE1 1DB London, United Kingdom.*

[5]*Department of Materials Science and Metallurgy, University of Cambridge, 27 Charles Babbage Road, Cambridge CB3 0FS, United Kingdom.*

[6]*Department of Physics and Astronomy, University College London, Gower Street, London WC1E 6BT, United Kingdom.*

† *These authors contributed equally.*

Nature controls the assembly of complex architectures through self-limiting processes, however few artificial strategies to mimic these processes have been reported to date. Here, we demonstrate a system comprised of two types of nanocrystals (NCs), where the self-limiting assembly of one NC component controls the aggregation of the other. Our strategy uses semiconducting InP/ZnS core-shell NCs (3 nm) as effective assembly-modulators and functional nanoparticle surfactants in cucurbit[*n*]uril-triggered aggregation of AuNCs (5-60 nm)

allowing rapid formation (seconds) of colloidally-stable hybrid aggregates. The resultant assemblies efficiently harvest light within the semiconductor substructures inducing out-of-equilibrium electron transfer processes, which can now be simultaneously monitored through the incorporated SERS–active plasmonic compartments. Spatial confinement of electron mediators (*e.g.* methyl viologen; MV^{2+}) within the hybrids enables the direct observation of photogenerated radical species as well as molecular recognition in real time, providing experimental evidence for the formation of elusive σ–$(MV^{+})_2$ dimeric species for the first-time. This approach paves the way for widespread use of analogous hybrids for long-term real-time tracking of interfacial charge-transfer processes, such as light-driven generation of radicals and catalysis with *operando* spectroscopies under irreversible conditions.

Colloidally-integrated hybrid nanostructures comprised of semiconductor and metal components are of great interest in materials development and application in next generation (photo)catalysis, optoelectronics, nanophotonics as well as drug-delivery, sensing and nanotheranostics.[1–3] To date, methods leading to assemblies based on nanocrystals (NCs) have relied on aggregation of constituent particles by attractive van der Waals[4] and anisotropic interactions,[5,6] electrostatic forces,[7] multitopic ligands,[8] biotin-streptavidin systems,[9] or DNA-based junctions.[10–13] These self-organisation processes usually require time-consuming evaporation of solvent or use of an antisolvent,[4,7] elevated temperature[4,5,7,10–13] and/or NC surface modification.[10–13] Moreover, once induced, self-assembly usually continues until the nanoparticulate components are consumed yielding crystals,[4,7,8,12] complex solids,[4,11] or amorphous precipitates.[4] Consequently, colloidal stabilisation of NC aggregates remains challenging and, for aqueous systems, particularly rare.[14–17]

A straightforward, yet unexplored, approach to control colloidal aggregates is through self-limiting assembly processes, where NC components can also play an active role in stabilising the resultant assemblies.[5,18] These processes consist of the assembly of NCs either solely[5] or supported by protein templates[19] and require temperature and/or pH modulation to trigger self-organisation (Figure 1a,b).[5,20,21] The resulting structures are comprised of one type of NC aggregate, however hybrids comprised of two or more types have not yet been achieved through self-limiting processes. Only recently has this approach been utilised to precisely spatially organise NCs yielding discrete clusters with molecule-like symmetry (Figure 1b).[22,23]

Employing the self-limiting assembly of one NC component to inherently control unlimited aggregation of another (Figure 1c) is conceptually different from currently reported systems. It would unveil a convenient method for facile hybridisation of NC constituents as well as kinetic entrapment of elusive aggregate phases.[24,25] Here, we introduce a strategy for kinetic arrest and stabilisation of metastable plasmonic assemblies within photo-active NC arrays through *interfacial self-limiting aggregation* (ISLA). This new hybridisation strategy relies on *molecular glue* mediated self-limiting assembly of semiconductor NCs at the interfaces of growing plasmonic NC aggregates. Semiconductor InP/ZnS core-shell NCs rapidly (seconds) modulate cucurbit[*n*]uril (CB[*n*])-triggered assembly of AuNCs,[26–28] passivating their interfaces and stabilising their kinetically-arrested states. Our room temperature approach results in colloidally-stable hybrids formed either from two types of aggregates (Figure 2a; pathway (*i*)) or well-dispersed metal NCs entrapped within semiconductor NC arrays (Figure 2a; pathway (*ii*)). The resulting hybrid assembly is permeable and able to efficiently absorb small molecules (such as electron mediators,

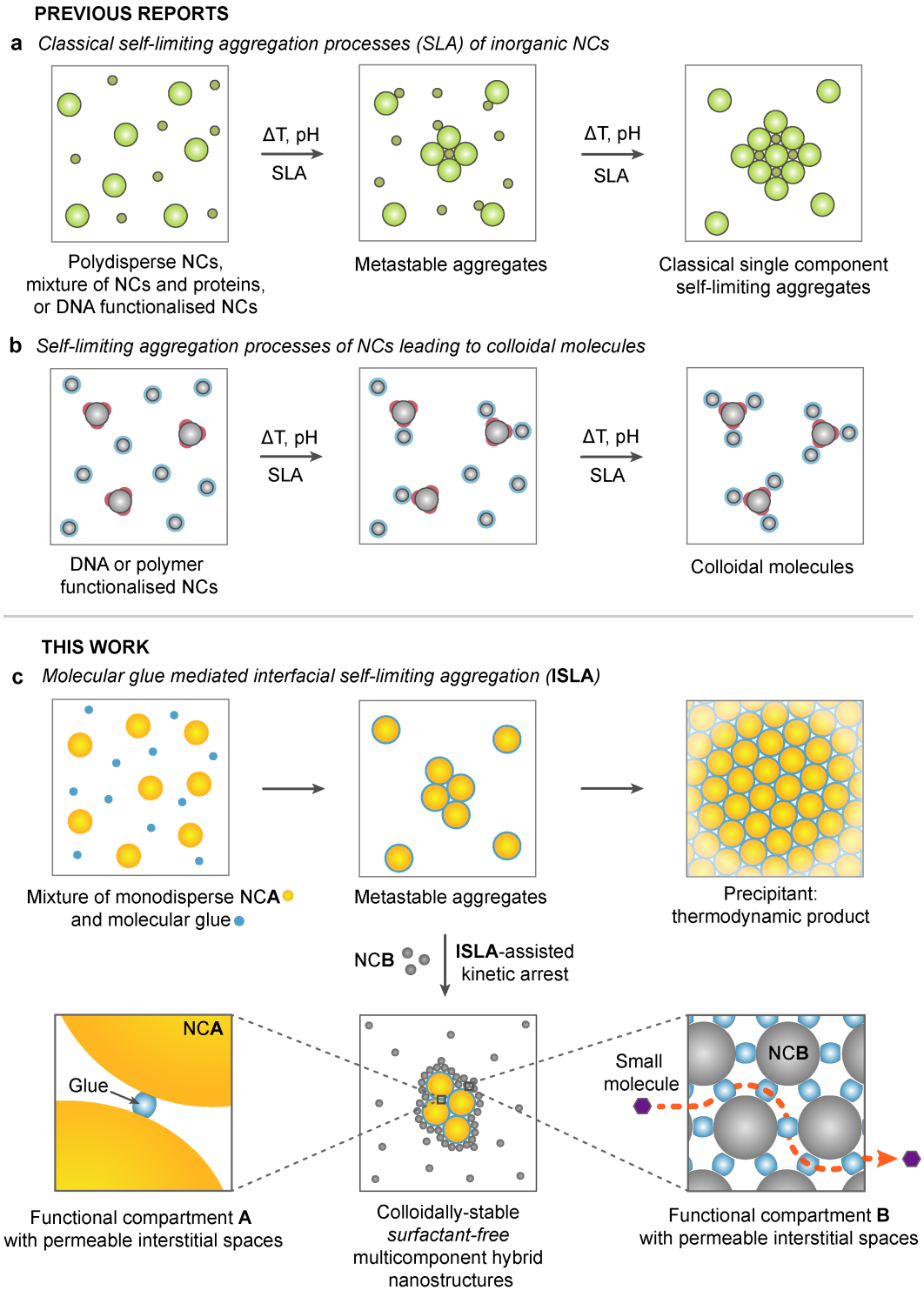

Figure 1: **Self-limiting assembly processes. a**, **b**, Previous reports. **c**, Novel strategy described here.

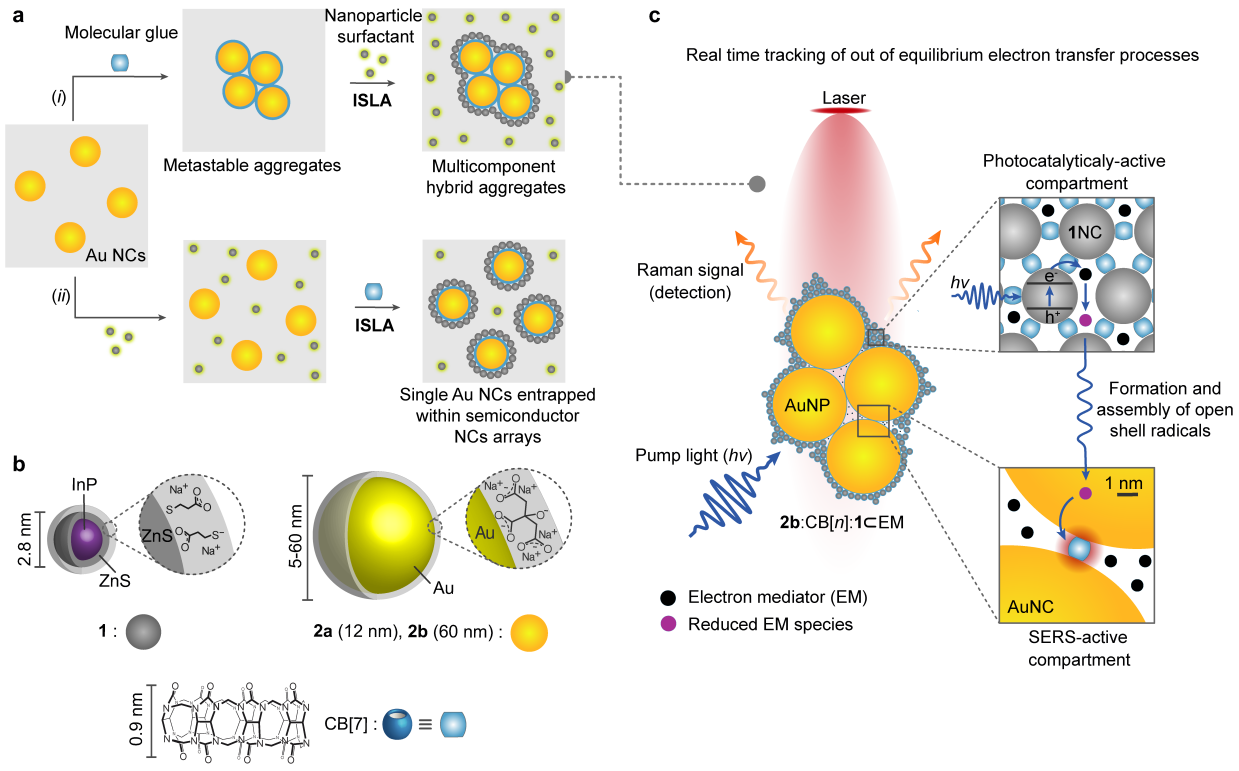

Figure 2: **Schematic representation of ISLA–assisted self-assembly processes of semiconductor/metal hybrids. a**, Interfacial self-limiting aggregation leading to (*i*) kinetic arrest of metastable plasmonic NC assemblies with functional colloidal surfactant and (*ii*) entrapment of single AuNCs within semiconductor NCs arrays. **b**, Building blocks used in the studies here. **c**, Schematics of bifunctional colloidally stable hybrid aggregates emphasising their photocatalytic and SERS-activity for real time tracking of interfacial electron transfer. These hybrids are: (*i*) chemically simple (since only the functional NCs and the molecular junction are involved) and (*ii*) permeable towards additional species in solution for subsequent chemistry (avoiding thick organic surfactant layers or inorganic silica shells).

Figure 2c) on account of the rigid CB[*n*] junction motifs that act as both a molecular glue and sub-nanometer separators, providing readily accessible interstitial spaces. As the hybrids consist of both photocatalytic and SERS-active components, they yield attractive opportunities for *in-situ* tracking of light-driven electron transfer processes confined at NC interfaces.

Molecular glue mediated self-limiting aggregation of InP/ZnS nanocrystals. InP/ZnS core-shell NCs (**1**; Figure 2b) stabilised by negatively-charged 3-mercaptopropionate species (3–MPA) were selected as a model chalcogenide to probe interactions with CB[n] macrocycles.[29,30] To explore kinetic entrapment of plasmonic aggregates, we employed AuNCs (**2a** and **2b**; Figure 2b) stabilised by citrate, which exhibit well-established optical properties and strong binding affinity to CB[n]s.[26–28,31] The NCs were monodisperse with inorganic core diameters of 2.8±0.5 nm (**1**), 12.0±0.9 nm (**2a**), and 60±2.4 nm (**2b**) and average hydrodynamic diameters (D_h) of 3.3±0.7 (**1**), 13.3±3.1 (**2a**), and 62.3±22.9 nm (**2b**) (Figures S1-S3 in the Supporting Information; SI). All NCs were water soluble, stable and did not aggregate when kept either in separate aqueous solutions or when mixed together in various ratios.

To investigate if CB[7] exhibits affinity to the NCs **1** interfaces, aqueous solutions of **1** and CB[7] are mixed together in various ratios (Figure 3a).[32] A highly luminescent flocculent material precipitates from solution in a few seconds when the ratio of CB[7]:**1** (χ) is 100 (Figure S4). The isolated solids, **1**:CB[7], consist of NCs of **1** with CB[7] and 3-MPA in an approximate ratio of $1_{\mathbf{1}}$:$20_{CB[7]}$:40_{3-MPA} as estimated by NMR and IR spectroscopies alongside elemental analysis (Figures S7-S9). Electron microscopy (TEM and STEM) reveals a loosely-packed open network structure of **1**:CB[7] precipitates (Figure S5).[33,34] Stable colloids of **1**:CB[7] (several weeks) are observed when the CB[7]:**1** ratio $N_{CB[7]}/N_{\mathbf{1}}=\chi<18$ (Figure 3a). For $18<\chi<25$ the solid product is only observed within a period of approximately 1 week (metastable suspension),[35] while precipitation of the aggregates becomes very rapid (visible aggregates <10s) when $\chi>50$. These experiments indicate that CB[7] chemisorbs readily to InP/ZnS NC **1** surfaces acting as a 'glue' to

efficiently bring together NCs forming an interconnected matrix.

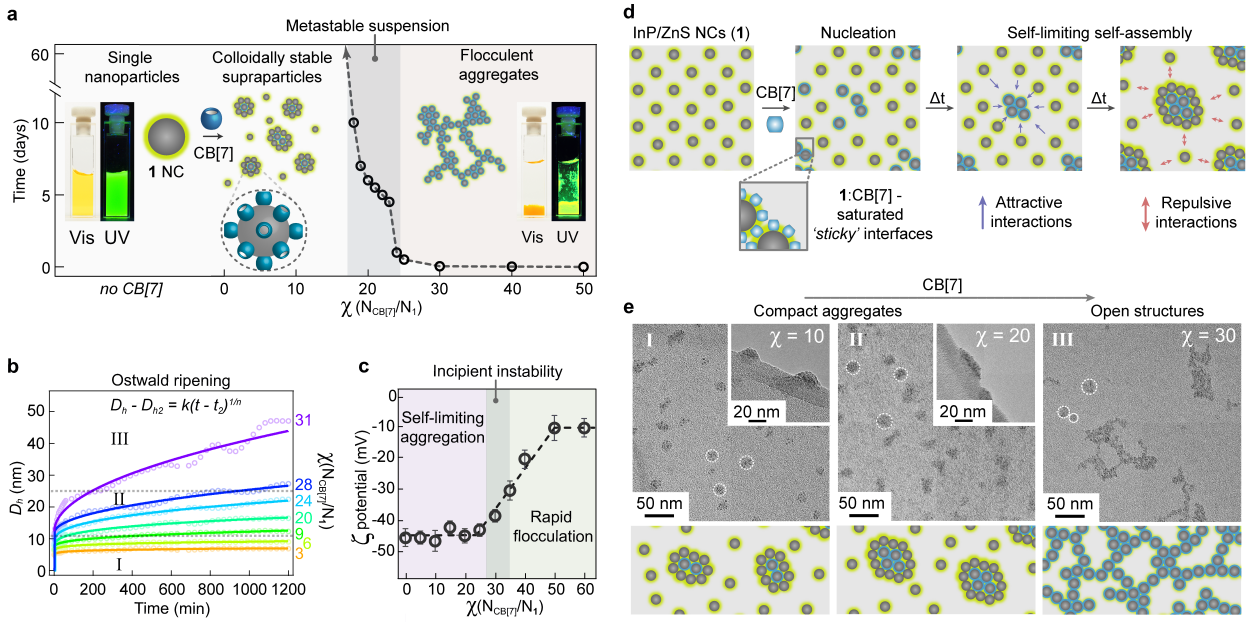

Figure 3: **Self-limiting self-assembly of InP/ZnS NCs and CB[7]. a**, Formation and stability of **1**:CB[7] assemblies *vs* ratio between number of CB[7] and **1** NCs. Time refers to a point until formation of observable precipitates was noted. **b**, Evolution of hydrodynamic diameter D_h in **1**:CB[7] monitored by DLS. **c**, Dependence of electrokinetic ζ potential on CB[7] to **1** NC ratio, χ ($N_{\mathbf{CB[7]}}/N_{\mathbf{1}}$), revealing the self-limiting character of aggregation for χ<20. **d**, Schematic representation of self-limiting processes leading to colloidally stable **1**:CB[7] assemblies. **e**, TEM micrographs of **1**:CB[7] aggregates for aliquots taken after 20 h of incubation.

To probe the assembly processes, the **1**:CB[7] system is monitored continuously using *in-situ* dynamic light scattering (DLS; Figures 3b, S11) and electrokinetic ζ potential measurements (Figure 3c) alongside TEM for various χ values (Figures 3e, S12). The size of the resultant aggregates can be tuned from bulk precipitates towards stable colloidal systems, as the concentration of CB[7] is reduced ($0<\chi<20$; Figures 3a-c). Controlling D_h of the **1**:CB[7] assemblies over a wide range (6–50 nm) is readily achieved through varying χ. Kinetic growth observed by DLS reveals two distinct stages of assembly, with initial fast growth after adding CB[7]. For example,

with χ=9 the D_h of **1**:CB[7] increases quickly from 3.3±0.7 to 9.3±2.8 nm within the first 5 min. After this initial stage, the growth slows by a factor of ≈100 leading to water-soluble assemblies with D_h = 11.8±3.0 nm after 20 h (Figure 3b).[36] The second stage of cluster growth fits the model of Ostwald ripening (Figure S14).[37] As χ approaches 20, assembly accelerates and systems with a higher CB[7] concentration reach the maximum D_h quicker; for χ>30 the colloids become unstable within 20 h.

The electrokinetic ζ potential experiments reveal the self-limiting nature of this CB[*n*]-mediated aggregation. The initial highly negative ζ potential of **1** (ζ=-45 mV) remains unchanged after addition of CB[7] if χ<20 (Figure 3c) indicating colloidal stability of emerging **1**:CB[7] assemblies as well as the self-limiting character of their growth.[5,38] For χ>20 a gradual increase in the ζ potential is observed reaching a moderate level (-30<ζ<-20 mV) for 30<χ<40 (incipient stability). Even less negative ζ potential values (ζ>–10 mV) are observed when χ>50 (unstable colloids).

The stability of the ζ potential and the ultimate cessation of aggregate growth for χ<20 can be rationalised by strong electrostatic repulsion both between emerging aggregates as well as aggregates and NCs of **1** (Figure 3d). In such systems (χ<20), smaller aggregates and/or free NCs take part in the stabilisation of larger assemblies, adhering to their 'sticky' interfaces saturated with CB[7] (inset in Figure 3d), screening attractive interactions between the latter and acting as dynamic particulate surfactants.[7,39–42] Saturation of the assembled interfaces with CB[7] macrocycles (χ>20) increases the probability of effective collisions, in which smaller aggregates become

glued to larger ones, decreasing the repulsive interactions and subsequently leading to flocculation and precipitation. These observations suggest that the colloidally stable **1**:CB[7] assemblies for χ<20 are likely a result of complex processes and a balance between many different factors, *i.e.* coordination and hydrogen bond-mediated attractive forces, van der Waals interactions, electrostatic repulsions as well as steric and entropic colloidal stabilisation.[43] On the contrary, for χ>20 the assembly processes change, becoming dominated by attractive forces when χ>40.

TEM images of stable suspensions of **1**:CB[7] provide structural insight into their morphology (Figures 3e, S12). Lower CB[7] concentrations (*i.e.* χ=10 and χ=20) leads to quasi-spherical loosely-packed clusters with mean diameters in good agreement with DLS. As the ratio of CB[7] is increased (χ>20) elongated chain-like fractal structures can be observed which are the dominant product when χ>30 (Figure 3e). This is likely explained by the assembly shifting from reaction-limited to diffusion-limited aggregation, which ultimately influences the final topology.[26]

Kinetic arrest of plasmonic assemblies through interfacial self-limiting aggregation (ISLA). The propensity of CB[7] to rapidly glue together NCs **1** was further exploited to kinetically arrest transient states of AuNC aggregates through interfacial self-limiting aggregation processes (ISLA) yielding hybrid semiconductor-metal nanoassemblies (Figure 4a).

In an initial experiment, CB[7] was added to a 1:1 v/v mixture of InP/ZnS NCs (10 μM; χ=100) and AuNCs **2a** (12 nm; 0.010 μM). This yielded red aggregates within seconds, which precipitated quantitatively after *ca.* 30 min (**2a**:CB[7]:**1**-Red; Figure S14). Alternatively, when CB[7] was first mixed with **2a**, followed by addition of **1** (all in the same ratios), a dark blue pre-

cipitate was observed (**2a**:CB[7]:**1**-Blue; Figure S16). TEM images of these two materials (Figures S15 and S17) highlight the structural differences. **2a**:CB[7]:**1**-Red contains single AuNCs, which are well dispersed throughout a loosely packed **1**:CB[7] matrix, while **2a**:CB[7]:**1**-Blue consists of chain-like assemblies of AuNCs trapped within **1**:CB[7] array. This set of experiments confirms that InP/ZnS NCs can be used as an efficient modulator of CB[*n*]-mediated aggregation of AuNCs.[26]

For direct monitoring of the ISLA-assisted assembly we employ larger AuNCs (**2b**; 60 nm) which offer good separation between UV-Vis absorption bands characteristic for monomers (localised surface plasmon resonance band, LSPR, at 535 nm, Figure 4b), dimers (660 nm), and large aggregates (680–900 nm).[26,44] The formation of colloidally-stable AuNC:CB[7]:InP/ZnSNC hybrids is comprehensively studied by UV-Vis spectroscopy, DLS, electrokinetic ζ potential, and electron microscopy experiments. The self-assembly of **2b**:CB[7]:**1** hybrids is triggered by the addition of CB[7] to a suspension of AuNCs (**2b**). The rate of aggregation is reflected in the progressive decrease of the LSPR band intensity of single AuNCs and subsequent appearance of dimer and long-chain modes (Figure 4b). Injection of **1** NCs[38] into the suspension during AuNC self-assembly leads to efficient arrest of the growth, trapping the **2b**:CB[7] aggregates within **1**:CB[7] arrays, visible by the stabilisation of the absorbance at 535 nm. Once **2b**:CB[7] assemblies are arrested, the resulting **2b**:CB[7]:**1** hybrids demonstrate extended stability of their optical properties for weeks, with no further changes observed in UV-Vis spectra (Figure 4b, S18; inset in Figure 4e). In contrast, in the absence of the InP/ZnS NCs, **2b**:CB[7] aggregates continue to grow resulting in precipitation after 30 – 60 min. The colloidal stability of the **2b**:CB[7] aggregates is shown by

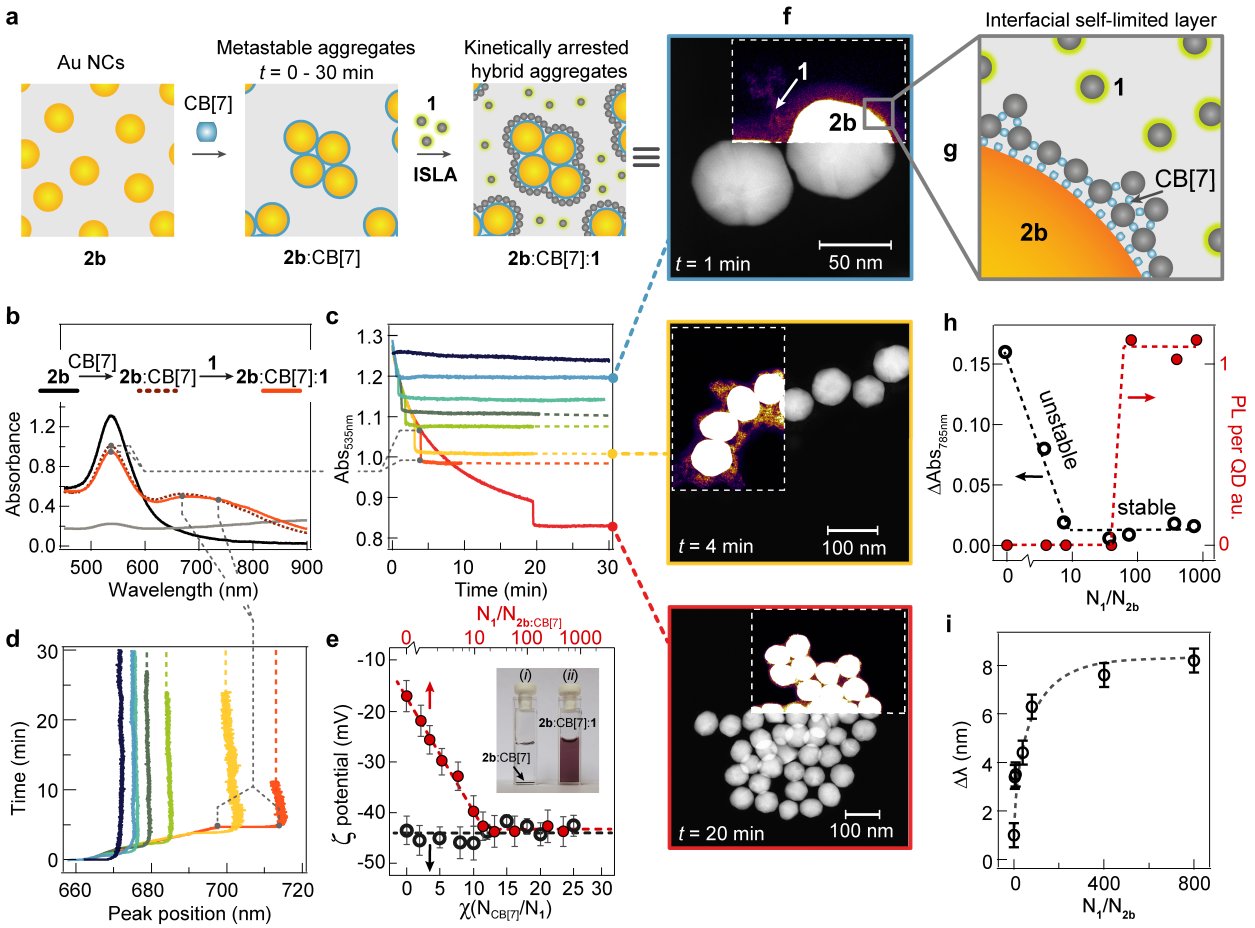

Figure 4: **Overview of kinetic arrest of plasmonic assemblies through interfacial self-limiting aggregation and the formation of hybrid systems.** **a**, Schematic representation of ISLA-mediated kinetic arrest of emerging AuNC aggregates and stabilisation of semiconductor-plasmonic hybrids. **b**, Typical UV-Vis spectra of: single AuNCs **2b** (black), **2b**:CB[7] aggregates after 10 min of CB[7]-mediated assembly (dashed orange), the same system just after injecting **1** to form **2b**:CB[7]:**1** hybrid (orange; note that this UV-Vis characteristic is retained for several weeks), and system of **2b** and CB[7] (no **1** NCs) after 30 min incubation (grey). **c**, Time-evolution of absorbance at 535 nm and **d**, spectral position of coupled mode resonance peak during **2b**:CB[7] aggregation with the addition of **1** at various time points. **e**, Changes in the electrokinetic ζ potential of **2b**:CB[7] aggregates upon addition of **1** (red); for $N_{\mathbf{1}}:N_{\mathbf{2b}:CB[7]}$ >20 the ζ potential values are characteristic for **1**:CB[7] aggregates from a self-limiting aggregation regime (black). **f**, Representative STEM images of **2b**:CB[7] aggregates entrapped within **1**:CB[7] arrays at different stages of aggregation; insets visualise **1**:CB[7] arrays by contrast colour-scaling. **g**, Schematics representing interfaces of the **2b**:CB[7]:**1** aggregates emphasising role of interfacial self-limited layer of **1**:CB[7] arrays. **h**, Evolution of coupled mode absorbance at 785 nm, 15 min after addition of **1** to **2b**:CB[7] (black) and normalised PL at 526 nm from 377 nm excitation (red) against number ratio between **1** and **2b** ($N_{\mathbf{1}}/N_{\mathbf{2b}}$). **i**, Spectral peak shift in the coupled mode resonance *vs* $N_{\mathbf{1}}/N_{\mathbf{2b}}$.

changes in ζ potential upon addition of **1**NCs (Figure 4e). Colloids of AuNCs **2b** are inherently stable with a ζ potential of -45 mV. The addition of relatively small quantities of CB[7] (*i.e.* 10^3 molecules per one **2b**NC; surface coverage $\approx$10%) destabilises the system leading to aggregation of the plasmonic NCs and an increase in ζ potential to -17 mV. The colloidal stability of the resultant system is restored by addition of **1**NCs ($>$20 per one **2b**NC), followed by changes in ζ potential to values characteristic of the starting materials, *ca.* -45 mV.

The size of these stable hybrids can be controlled by adding **1** at a specific time, once a desired level of **2b**:CB[7] aggregation is reached (Figures 4c, d). The typical morphology of the resulting **2b**:CB[7]:**1** hybrids is visualised using electron microscopy (Figure 4f, S19), revealing individual AuNC aggregates decorated with **1**NCs. For example, dimeric species are observed as the main fraction of the system when aggregation is stopped after 60 s (Figure 4f, top). Larger assemblies, typically incorporating 4-8 or 20-40 NCs of **2b**, are found for systems in which growth was terminated after 4 and 20 min, respectively.[45] This is on account of the rapid formation of a CB[7]:**1** layer through self-limiting processes at interfaces of **2b**:CB[7] aggregates (Figure 4g, 4f), preventing attractive interactions between **2b**:CB[7] cores. In these systems the InP/ZnS NCs can be regarded as stabilising surfactants,[7,39–42] which absorb excess CB[7] molecules and passivate the interfaces of AuNC:CB[7] assemblies, halting further aggregation.

Evolution of the refractive index (RI) and the optical properties of the AuNC aggregates upon addition of **1** provides further insight into the interfacial composition of the **2b**:CB[7]:**1** hybrids (Figure 4c-d, h-i and S20-21). The redshift of the coupled mode resonance (*ca.* 785 nm) of

2b:CB[7] assemblies (Figure 4c,i) reflects an increase of their surrounding RI and is a direct indication of the decoration of the AuNC surfaces with high RI semiconductor NCs (RI_{InP} = 2.4).[46,47] Moreover, monitoring the evolution of the coupled mode absorbance at 785 nm for the systems with different **1**:**2b** ratios ($N_{\mathbf{1}}/N_{\mathbf{2b}}$) shows that stabilisation of the optical properties of the **2b**:CB[7] aggregates is achieved for $N_{\mathbf{1}}/N_{\mathbf{2b}}>10$ (Figure 4h); in line with electrokinetic ζ potential measurements, which indicate recovery of colloidal stability for $N_{\mathbf{1}}/N_{\mathbf{2b}}>20$ (Figure 4e).

Tracking light-driven out of equilibrium redox chemistry at nanoparticle interfaces. Spatial confinement of the photocatalytically-active InP/ZnS NCs **1** with plasmonic AuNC antennae **2b** (Figure 5a) was explored as a multifunctional colloidal substrate for real-time observation of photogenerated radical species *via operando* surface enhanced Raman spectroscopy (SERS).

Methyl viologen, MV^{2+}, was selected as a model electron acceptor on account of its well-studied redox chemistry (Figure 5b) and Raman activity.[48,49] The one-electron reduction of MV^{2+} to a radical cation, $MV^{+\cdot}$, makes it an efficient electron mediator (EM), attracting enormous attention for photocatalysis, electrochromic devices, solar energy conversion systems, batteries, and molecular machines.[48–52] However, despite their widespread application and extensive reports on their redox properties, the assembly of $MV^{+\cdot}$ radicals and structures of the resultant dimeric species remain poorly understood. Geraskina *et al.* recently reported that MV sigma dimers (4,4', 2,2', and 2,4; Figure 5b) could not be formed under thermodynamic conditions on account of extremely high calculated free energies of binding.[53] Herein we report, to the best of our knowledge, the first direct observation of the formation of MV sigma dimers under out-of-equilibrium conditions at

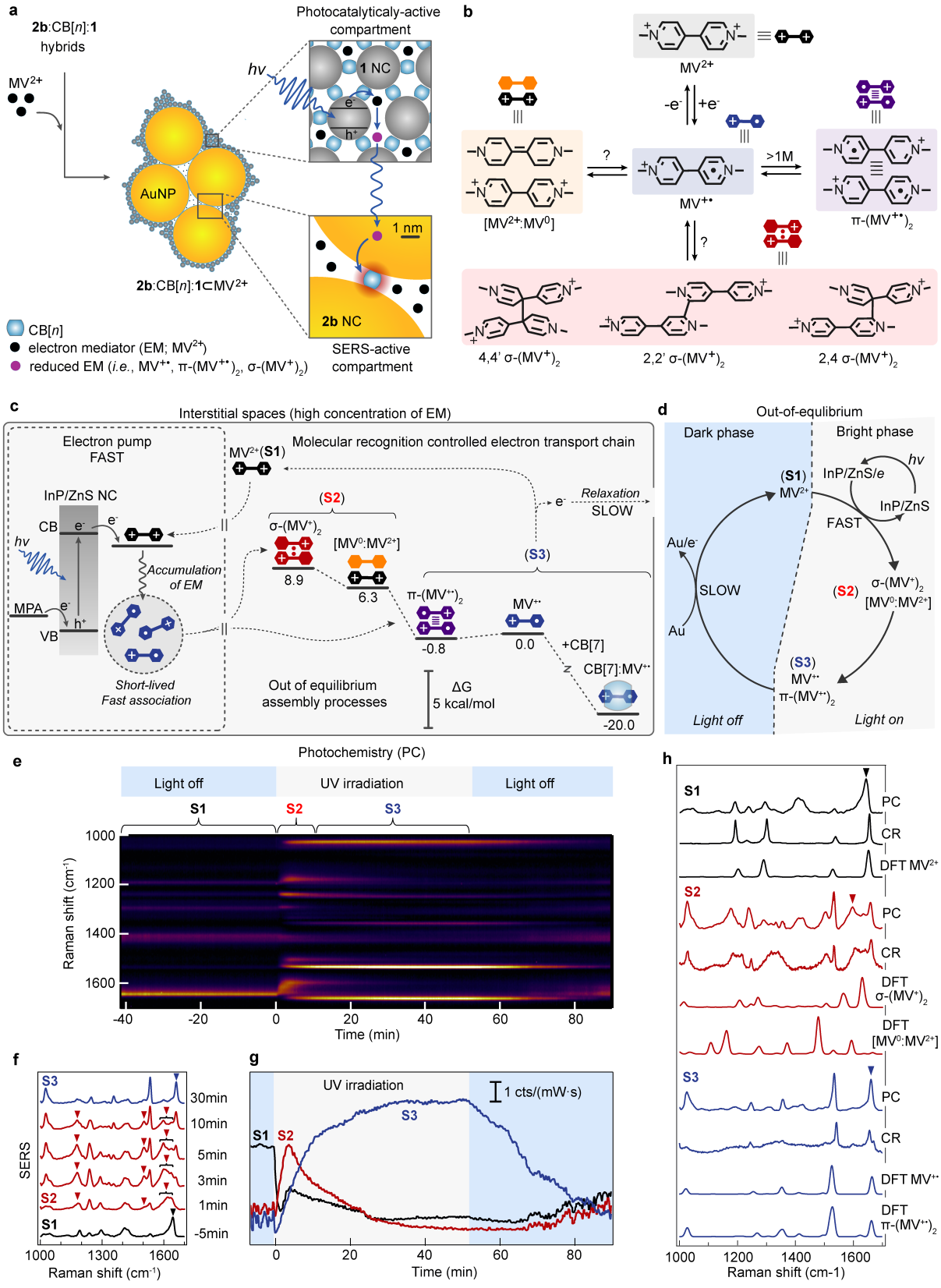

Figure 5: **Tracking light-driven out of equilibrium redox chemistry within the hybrid aggregates.** (Continued on the next page.)

Figure 5: **a**, Schematic representation of the hybrid aggregates emphasising role of their compartmentalisation and sorption capabilities. **b**, Redox chemistry of methyl viologen as molecular electron mediator (EM). **c**, Out of equilibrium electron transfer within the hybrids with free energies of binding for all of the observed products depicting significance of molecular recognition for controlling of these processes. InP/ZnS NCs **1** - mediated light-induced electron reduction of MV^{2+} (state **S1**) leads to the formation of $MV^{+\cdot}$ radicals, which undergo further fast association processes to form elusive σ-$(MV^{+})_2$ and $[MV^{2+}{:}MV^{0}]$ species (state **S2**) and classical π-$(MV^{+\cdot})_2$ dimers (state **S3**). Dissociation of the dimeric species is promoted by encapsulation of $MV^{+\cdot}$ within CB[7] macrocycles. The $MV^{+\cdot}$ can further slowly relax by oxidation reactions to regenerate MV^{2+} species. **d**, A photochemical cycle within the hybrids and its division to *bright* and *dark* phases. **e**, Real-time SERS monitoring of MV^{2+} photochemistry (PC) within the hybrid aggregates, with UV irradiation time period marked with a blue bar. **f**, Selected spectra from the photochemistry SERS time scan showing the distinct spectra for the three different states. Triangles mark the diagnostic peak positions representative for each species used for fitting; respective time stamps are displayed on the right axis. **g**, Photochemical kinetics of each species (**S1** , black: MV^{2+} 1643 cm^{-1}; **S2**, red: σ-$(MV^{+})_2$/$[MV^{2+}{:}MV^{0}]$ 1600 cm^{-1}; and **S3**, blue: $MV^{+\cdot}$/π-$(MV^{+\cdot})_2$ 1660 cm^{-1}) extracted through multi-Gaussian fitting. **h**, Comparison of spectra obtained from photochemistry (PC), chemical reduction (CR), and DFT calculations for different MV species.

room temperature using **2b**:CB[7]:**1** assemblies.

The hybrid aggregates incorporating MV^{2+} were prepared by simple addition of the EM (MV^{2+}) to a deoxygenated aqueous suspension of **2b**:CB[7]:**1** ($C_{\mathbf{MV}^{2+}}$ = 1.6 μM; MV^{2+}:CB[n] molar ratio 1:1). MV^{2+} adsorbs to the **2b**:CB[7]:**1** interfaces (Figure S43) with an estimated surface density of one MV^{2+} molecule per 5 nm^2 to form a **2b**:CB[7]:**1**$\subset MV^{2+}$ supramolecular system. The resultant stable suspension was uniformly illuminated with excitation at λ = 302 nm (*pump light*, generating excited electrons within NC **1**), while *operando* SERS was probed using a 785 nm laser (*probe light*; Figure S42).

An overview of the photo-induced interfacial transformations are shown in Figure 5c and 5d.

Photo-irradiation of the **2b**:CB[7]:**1**⊂MV^{2+} system generates high energy electrons within NC **1**, which are immediately transferred to chemisorbed MV^{2+} (state 1; **S1**), undergoing reduction to form $MV^{+\cdot}$ monoradical cations. The initial high local concentration and spatial confinement of the photo-generated products promote their fast (below temporal resolution of the instrument) association leading to the formation of elusive σ–$(MV^{+})_2$ dimeric species and [MV^{2+}:MV^{0}] heterobinary complexes (state 2; **S2**) as well as classical π–$(MV^{+\cdot})_2$ dimers and monoradical $MV^{+\cdot}$ cations (state 3; **S3**).[53] Both of the dimeric species undergo further dissociation to form $MV^{+\cdot}$ which, in the case of **2b**:CB[7]:**1**, is promoted by their encapsulation within the CB[7] cavity to form thermodynamically stable 1:1 complexes.[54] Before ultimately returning to their ground state, the photogenerated radicals can relax through donating an electron to the Fermi level in AuNCs **2b**.[55] Notably, the photo-generation of the $MV^{+\cdot}$ should be characterised by different reaction rates in comparison to the AuNC mediated relaxation; therefore, two distinct phases of non-equilibrium processes are anticipated (Figure 5d): (*i*) a photo-driven *bright phase* leading to accumulation of photo-generated products, and (*ii*) a *dark phase* controlled by the relaxation processes.

The kinetics of these photochemical processes are directly revealed through real-time SERS spectra (Figure 5e-h). The attribution of the observed sets of vibrational peaks is supported by density functional theory (DFT) calculations and, where possible, by Raman spectroscopy experiments for bulk aqueous MV^{2+} solutions in the absence and presence of a chemical reducing agent (Figure 5h and S45, S46 in SI). In the absence of UV irradiation (from t=-40 to t=0 min; Figure 5e), the SERS intensity of MV^{2+} (**S1**; assigned diagnostic peak at 1643 cm^{-1}) is found to be stable under exposure to the 785 nm probe laser. Introduction of the *pump light* (λ=302 nm) leads to the

evolution of three specific states (**S1**–**S3**) with distinct spectral features (Figure 5e-g).[56] An immediate decrease in the SERS intensity of MV^{2+} is first observed, accompanied with corresponding intensity increases from SERS bands attributed to a mixture of $MV^{+\cdot}$ and π–$(MV^{+\cdot})_2$ (**S3**), denoted by diagnostic Raman resonance at 1660 cm^{-1}. Interestingly, additional bands are observed between 1600 cm^{-1} and 1640 cm^{-1} as well as at 1504 cm^{-1} and 1180 cm^{-1} (Figure 5f), which have a different kinetic profile from states **S1** and **S3**. These bands were attributed to the elusive dimeric species connected by a sigma bond, σ–$(MV^{+})_2$, as well as the $[MV^{2+}{:}MV^{0}]$ pair[57,58] (**S2**), corroborated by DFT calculations (Figures 5h and S29, S46 in SI).[56] Signals characteristic for state **S2** saturate after 4 min, which is followed by a decrease in their intensity, indicating the dominance of dissociation of the σ–$(MV^{+})_2$ dimer and comproportionation[59] of the $[MV^{2+}{:}MV^{0}]$ species. Both these processes further contribute to the population of $MV^{+\cdot}$ radical cations, increasing their concentration before reaching saturation (t=35 min). In the described **2b**:CB[7]:**1** system, decreasing concentrations of σ–$(MV^{+})_2$ and $[MV^{2+}{:}MV^{0}]$ result from efficient encapsulation of $MV^{+\cdot}$ radical cations within CB[7],[54] which shifts the local equilibrium towards the monomeric MV states as corroborated by free energy of binding calculations (ΔG; Figures 5c and S24-S39). Upon removal of the pump light, the system is switched from an out-of-equilibrium light-driven phase (*bright phase*; Figure 5c) to an equilibrated state (*dark phase*). This is associated with a decrease in intensity of the $MV^{+\cdot}$ signal and a corresponding increase in intensity of the MV^{2+} signal, a result of the relaxation of the system. [55]

Supramolecular control of light-induced redox-driven processes at colloidal interfaces. Variation of the CB[*n*] (*n* = 5-8) cavity size can control binding and complexation of analytes as a

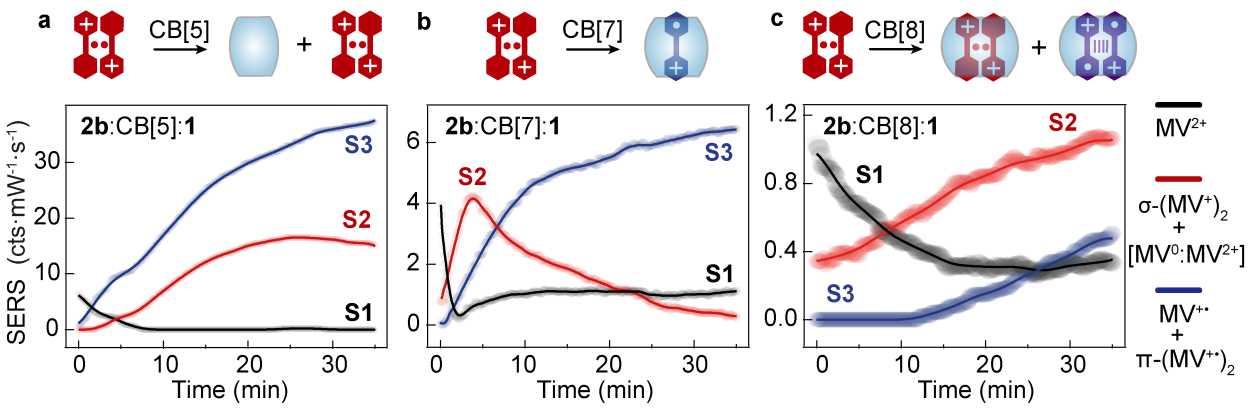

Figure 6: **Real-time monitoring of light-induced redox-driven molecular recognition processes.** Photochemical kinetics of each species extracted through multi-Gaussian fitting for: **a**, **2b**:CB[5]:**1**. **b**, **2b**:CB[7]:**1**. **c**, **2b**:CB[8]:**1**.

function of the homologue. The cavity of CB[5], for example, is too small to accommodate any viologen derivative.[27] Therefore, when CB[5] is employed as the gluing agent (**2b**:CB[5]:**1**⊂MV^{2+}), all of the light-induced chemical processes occur outside the cavity. We anticipated that in such a system the lifetime of the photo-generated σ–$(MV^{+})_2$ dimers and [MV^{2+}:MV^{0}] species will be increased in comparison to the hybrids based on the larger CB[7] macrocycle. Indeed, for the CB[5]-based system, a signal decrease for MV^{2+} is observed upon UV irradiation, which is accompanied with a rise in the SERS intensity from σ–$(MV^{+})_2$/[MV^{2+}:MV^{0}] (**S2**), and $MV^{+\cdot}$/ π–$(MV^{+\cdot})_2$ (**S3**) (Figure 6a and S44 in SI). Notably, signals from state **S2** are found to be relatively stable, saturating after *ca.* 25 min, highlighting that when out-of-equilibrium reaction conditions are applied (*bright phase*) the thermodynamically unstable σ–$(MV^{+})_2$ and [MV^{2+}:MV^{0}] species can accumulate within the hybrid aggregates.

In contrast, the CB[7] spacer has a large enough cavity to encapsulate a single MV^{2+}, $MV^{+\cdot}$ or MV^{0} species forming binary 1:1 host-guest complexes.[54] Within CB[7]-bridged **2b**:CB[7]:**1**⊂MV^{2+}

hybrid aggregates, formation of the dimeric species is suppressed, which is reflected by the early saturation point of **S2** (Figure 6b; t=4 min). In this system, CB[7] macrocycles promote dissociation of the σ–$(MV^{+})_2$ dimers and the [MV^{2+}:MV^{0}] pair by sequestering $MV^{+\cdot}$ radical cations within their molecular cavities.

The larger CB[8] homologue not only accommodates MV^{2+} within a 1:1 host-guest complex, but also enhances dimerisation of $MV^{+\cdot}$ through encapsulation. Indeed, within a hybrid aggregate held together with CB[8] (**2b**:CB[8]:**1**$\subset MV^{2+}$), continuous generation of dimeric species is observed from the onset of photoexcitation (Figure 6c and S44). Notably, the appearance of signals characteristic for $MV^{+\cdot}$/ π–$(MV^{+\cdot})_2$ (**S3**) is significantly delayed and occur after only 12 min. This is likely a result of retaining stabilised σ–$(MV^{+})_2$ dimers (Figure 5j) within CB[8] in the first stage of the *bright phase* and thus subsequent suppression of $MV^{+\cdot}$ population (Figure 6c).

Conclusions. We demonstrate a new assembly strategy leading to photoactive colloidally-stable hybrid materials consisting of semiconductor and plasmonic NCs. Rapid hybridisation is accomplished through interfacial self-limiting aggregation (ISLA) of semiconductor NCs, which adsorb at the surfaces of growing AuNC aggregates through sub-nanometer CB[n] (n = 5-8) molecular bridges. As CB[n] is able to mediate the assembly of both semiconductor and plasmonic NCs, a wide array of new hybrid systems can be readily prepared with implicit control over morphology and optical properties. These systems harvest light efficiently within the semiconductor substructures, inducing out-of-equilibrium electron transfer processes, the products of which can be simultaneously detected through the incorporated SERS-active AuNC antennae. This functional compartmentalisation alongside spatial confinement of an electron mediator, methyl viologen (MV^{2+}),

within the interstitial spaces of the hybrids enables direct observation of various out-of-equilibrium photochemical transformations in real time. The light-controlled generation of MV radical species and their subsequent assembly directed by molecular recognition driven intermolecular electron transfer reveals the formation of the long overlooked elusive σ–$(MV^{+})_2$ dimeric species. The impressive colloidal stability, dynamic character, and permeability of the CB[n]-bridged hybrid constructs enabled, for the first time, *in situ* tracking of complex chemistries of open shell radicals strictly controlled by host-guest interactions. As our strategy reveals exclusively chemical species confined within the aggregates and located in close proximity to AuNC surfaces ($<$2 nm), the reported hybrid systems can also be regarded as a prototypical colloidal nano(photo)electrode, serving as a powerful platform for the direct and precise visualisation of redox chemistry at metal/water and semiconductor/water interfaces. These findings pave the way for widespread use of such hybrids for long-term, real-time tracking of interfacial charge-transfer processes, *i.e.* light-driven generation of radicals and catalysis with *operando* spectroscopies under out of equilibrium conditions.

Acknowledgements We acknowledge financial support from EPSRC Grants EP/L027151/1 (NOtCH) and EP/R020965/1 (RaNT). J.H. thanks support from Chinese Scholarship Council and Cambridge Commonwealth, European and International Trust. B.d.N. acknowledges support from the Leverhulme Trust and Isaac Newton Trust. S.M.C. thanks Girton College, Cambridge for a Henslow Research Fellowship. We thank Dr Steven J. Barrow, Dr Alexander S. Groombridge and Dr István Szabó for helpful discussions. The authors acknowledge use of the research computing facility at King's College London, Rosalind (https://rosalind.kcl.ac.uk).

Competing Interests The authors declare that they have no competing financial interests.

Correspondence Correspondence and requests for materials should be addressed to Oren A. Scherman (email: oas23@cam.ac.uk).

Data Availability Methods and materials characterisation are provided in the Supplementary Information. The data that support the findings of this study are available from the corresponding author on reasonable request.

References

1. Jiang, R., Li, B., Fang, C. & Wang, J. Metal/semiconductor hybrid nanostructures for plasmon-enhanced applications. *Adv. Mater.* **26**, 5274–5309 (2014).

2. Lim, E.-K. *et al.* Nanomaterials for theranostics: Recent advances and future challenges. *Chem. Rev.* **115**, 327–394 (2015).

3. Boles, M., Engel, M. & Talapin, D. Self-assembly of colloidal nanocrystals: From intricate structures to functional materials. *Chem. Rev.* **116**, 11220–11289 (2016).

4. Boles, M., Ling, D., Hyeon, T. & Talapin, D. The surface science of nanocrystals. *Nat. Mater.* **15**, 141–153 (2016).

5. Xia, Y. *et al.* Self-assembly of self-limiting monodisperse supraparticles from polydisperse nanoparticles. *Nat. Nanotechnol.* **6**, 580–587 (2011).

6. Glotzer, S. & Solomon, M. Anisotropy of building blocks and their assembly into complex structures. *Nat. Mater.* **6**, 557–562 (2007).

7. Kalsin, A. *et al.* Electrostatic self-assembly of binary nanoparticle crystals with a diamond-like lattice. *Science* **312**, 420–424 (2006).

8. André, A. *et al.* Toward conductive mesocrystalline assemblies: PbS nanocrystals cross-linked with tetrathiafulvalene dicarboxylate. *Chem. Mater.* **27**, 8105–8115 (2015).

9. Connolly, S. & Fitzmaurice, D. Programmed assembly of gold nanocrystals in aqueous solution. *Adv. Mater.* **11**, 1202–1205 (1999).

10. Macfarlane, R., O'Brien, M., Petrosko, S. & Mirkin, C. Nucleic acid-modified nanostructures as programmable atom equivalents: forging a new "table of elements". *Angew. Chem. Int. Ed.* **52**, 5688–5698 (2013).

11. Lin, H. *et al.* Clathrate colloidal crystals. *Science* **355**, 931–935 (2017).

12. Park, D. *et al.* Plasmonic photonic crystals realized through dna-programmable assembly. *Proc. Natl. Acad. Sci. U.S.A.* **112**, 977–981 (2015).

13. Wang, R., Nuckolls, C. & Wind, S. Assembly of heterogeneous functional nanomaterials on DNA origami scaffolds. *Angew. Chem. Int. Ed.* **51**, 11325–11327 (2012).

14. Wang, Y. *et al.* Host-guest chemistry with water-soluble gold nanoparticle supraspheres. *Nat. Nanotechnol.* **12**, 170–176 (2017).

15. Sánchez-Iglesias, A. *et al.* Hydrophobic interactions modulate self-assembly of nanoparticles. *ACS Nano* **6**, 11059–11065 (2012).

16. Choueiri, R. M., Klinkova, A., Thérien-Aubin, H., Rubinstein, M. & Kumacheva, E. Structural transitions in nanoparticle assemblies governed by competing nanoscale forces. *J. Am. Chem. Soc.* **135**, 10262–10265 (2013).

17. Wang, T., LaMontagne, D., Lynch, J., Zhuang, J. & Cao, Y. C. Colloidal superparticles from nanoparticle assembly. *Chem. Soc. Rev.* **42**, 2804–2823 (2013).

18. Jia, G. *et al.* Couples of colloidal semiconductor nanorods formed by self-limited assembly. *Nat. Mater.* **13**, 301–307 (2014).

19. de Q. Silveira, G. *et al.* Supraparticle nanoassemblies with enzymes. *Chem. Mater.* **31**, 7493–7500 (2019).

20. Li, F., Josephson, D. P. & Stein, A. Colloidal assembly: The road from particles to colloidal molecules and crystals. *Angew. Chem. Int. Ed.* **50**, 360–388 (2011).

21. Banin, U. & Sitt, A. Colloidal self-assembly: Superparticles get complex. *Nat. Mater.* **11**, 1009–1011 (2012).

22. Yi, C. *et al.* Self-limiting directional nanoparticle bonding governed by reaction stoichiometry. *Science* **369**, 1369–1374 (2020).

23. Yao, G. *et al.* Programming nanoparticle valence bonds with single-stranded dna encoders. *Nature Materials* **19**, 781–788 (2020).

24. Leukel, S. *et al.* Trapping amorphous intermediates of carbonates - a combined total scattering and NMR study. *J. Am. Chem. Soc.* **140**, 14638–14646 (2018).

25. Jehannin, M., Rao, A. & Cölfen, H. New horizons of nonclassical crystallization. *J. Am. Chem. Soc.* **141**, 10120–10136 (2019).

26. Taylor, R. *et al.* Precise subnanometer plasmonic junctions for SERS within gold nanoparticle assemblies using cucurbit[*n*]uril "glue". *ACS Nano* **5**, 3878–3887 (2011).

27. Barrow, S., Kasera, S., Rowland, M., Del Barrio, J. & Scherman, O. A. Cucurbituril-based molecular recognition. *Chem. Rev.* **115**, 12320–12406 (2015).

28. Chikkaraddy, R. *et al.* Single-molecule strong coupling at room temperature in plasmonic nanocavities. *Nature* **535**, 127–130 (2016).

29. Jing, L. *et al.* Aqueous based semiconductor nanocrystals. *Chem. Rev.* **116**, 10623–10730 (2016).

30. Ni, X.-L. *et al.* Cucurbit[*n*]uril-based coordination chemistry: From simple coordination complexes to novel poly-dimensional coordination polymers. *Chem. Soc. Rev.* **42**, 9480–9508 (2013).

31. Al-Johani, H. *et al.* The structure and binding mode of citrate in the stabilization of gold nanoparticles. *Nat. Chem.* **9**, 890–895 (2017).

32. For the experiments described herein we have chosen CB[7], however we note that other CB[*n*] homologues work similarly.

33. Ziegler, C. *et al.* Modern inorganic aerogels. *Angew. Chem. Int. Ed.* **56**, 13200–13221 (2017).

34. Hendel, T. *et al.* Mixed aerogels from Au and CdTe nanoparticles. *Adv. Funct. Mater.* **23**, 1903–1911 (2013).

35. We note that the CB[7]:**1** ratios found for the isolated solids (χ = 20) are independent of the amount of CB[7] used (Figure S8) and consistent with the empirically found minimum amount of CB[7] required to induce precipitation of **1**:CB[7] systems (χ = 18; Figure 1c).

36. We note, that the aggregation processes expressed by changes in the measured hydrodynamic diameter can be an effect of complex processes involving not only evolution of size but also changes in shape of the emerging clusters.

37. Huang, F., Zhang, H. & Banfield, J. F. Two-stage crystal-growth kinetics observed during hydrothermal coarsening of nanocrystalline ZnS. *Nano Lett.* **3**, 373–378 (2003).

38. Number ratio between **1** and **2b**, $n_{\mathbf{1}}/n_{\mathbf{2a}} = 10^4$, is used to ensure **2b** interfaces are covered by **1** NCs.

39. Yang, Z., Wei, J., Sobolev, Y. I. & Grzybowski, B. A. Systems of mechanized and reactive droplets powered by multi-responsive surfactants. *Nature* **553**, 313–318 (2018).

40. Kowalczyk, B. *et al.* Charged nanoparticles as supramolecular surfactants for controlling the growth and stability of microcrystals. *Nat. Mater.* **11**, 227–232 (2012).

41. Liu, X. *et al.* Reconfigurable ferromagnetic liquid droplets. *Science* **365**, 264–267 (2019).

42. Cui, M., Emrick, T. & Russell, T. P. Stabilizing liquid drops in nonequilibrium shapes by the interfacial jamming of nanoparticles. *Science* **342**, 460–463 (2013).

43. Silvera Batista, C. A., Larson, R. G. & Kotov, N. A. Nonadditivity of nanoparticle interactions. *Science* **350**, 176–187 (2015).

44. We note that control over optical properties and colloidal stability is also demonstrated for 5 nm and 12 nm Au NCs (see Figures S23 and S24).

45. Morphology of the Au:CB[n]:InP/ZnS hybrids is determined by the structure of central plasmonic component whose growth is kinetically arrested by the addition of NCs **1**. Kinetically arrested states are typically less uniform in comparision to thermodynamically controlled structures. However, here the reported processes allow for facile and effective stabilisation of optical properties of the plasmonic component while providing outstanding colloidal stability and structure permeability for photochemistry .

46. Homola, J. Surface plasmon resonance sensors for detection of chemical and biological species. *Chem. Rev.* **108**, 462–493 (2008).

47. Wang, Y. *et al.* Self-assembly and structure of directly imaged inorganic-anion monolayers on a gold nanoparticle. *J. Am. Chem. Soc.* **131**, 17412–17422 (2009).

48. Monk, P. M. S. *The Viologens: Physicochemical Properties, Synthesis and Applications of the Salts of 4,4'-Bipyridine* (WILEY-VCH Verlag GmbH, 1999).

49. Striepe, L. & Baumgartner, T. Viologens and their application as functional materials. *Chem. Eur. J.* **23**, 16924–16940 (2017).

50. McCune, J. A., Kuehnel, M. F., Reisner, E. & Scherman, O. A. Stimuli-mediated ultrastable radical formation. *Chem* **6**, 1819 – 1830 (2020).

51. Trabolsi, A. *et al.* Radically enhanced molecular recognition. *Nat. Chem.* **2**, 42–49 (2010).

52. Bruns, C. J. & Stoddart, J. F. *The Nature of the Mechanical Bond: From Molecules to Machines.* (WILEY-VCH Verlag GmbH, 2016).

53. Geraskina, M., Dutton, A., Juetten, M., Wood, S. & Winter, A. The viologen cation radical pimer: A case of dispersion-driven bonding. *Angew. Chem. Int. Ed.* **56**, 9435–9439 (2017).

54. Kim, H.-J., Jeon, W. S., Ko, Y. H. & Kim, K. Inclusion of methylviologen in cucurbit[7]uril. *Proc. Natl. Acad. Sci. U.S.A.* **99**, 5007–5011 (2002).

55. Meisel, D., Mulac, W. A. & Matheson, M. S. Catalysis of methyl viologen radical reactions by polymer-stabilized gold sols. *J. Phys. Chem.* **85**, 179–187 (1981).

56. We note that state **s2** can be further deconvoluted revealing additional kinetics, which are similar yet distinguishable from each other (see Figure S47 in the SI and the discussion thereof).

57. We note that the formation of [MV^{2+}:MV^{0}] binary complex can result from disproportionation of $MV^{+\cdot}$ radicals spacially confined within the hybrid aggregates. For a previous report regarding redox processes of $MV^{+\cdot}$ radicals leading to the formation of pairs consisting of neutral and native non-reduced viologens, [MV^{2+}:MV^{0}], in solid-state system characterised by X-ray diffraction crystallography, please see J. Org. Chem. 55, 4127-4135 (1990).

58. Bockman, T. M. & Kochi, J. K. Isolation and oxidation-reduction of methylviologen cation radicals. Novel disproportionation in charge-transfer salts by X-ray crystallography. *J. Org. Chem.* **55**, 4127–4135 (1990).

59. Norton, J. D. & White, H. S. Effect of comproportionation on the voltammetric reduction of methyl viologen in low ionic strength solutions. *J. Electroanal. Chem.* **325**, 341 – 350 (1992).